



Applied Catalysis B: Environmental

journal homepage: www.elsevier.com/locate/apcatb

Visible-light-driven photocatalytic properties of ZnO/ZnFe₂O₄ core/shell nanocable arrays

Xuan Guo, Haojun Zhu, Quan Li*

Department of Physics, The Chinese University of Hong Kong, Shatin, New Territories, Hong Kong

ARTICLE INFO

Article history:

Received 8 November 2013

Received in revised form 17 April 2014

Accepted 26 May 2014

Available online 2 June 2014

Keywords:

Visible-light-driven photocatalysis

Zinc ferrites

Nanocable arrays

ZnO-nanowire-array template

Type II band alignment

ABSTRACT

ZnO-core/ZnFe₂O₄-shell nanocable arrays on the sapphire substrate were grown using a simple sacrificial ZnO-nanowire-array templating method. When comparing to pure ZnO nanowire arrays (the “core” only) or ZnFe₂O₄ nanotube arrays (the “shell” only), the ZnO/ZnFe₂O₄ nanocable arrays have demonstrated the highest photodegradation capability of rhodamine B (RhB) under visible light illumination. Although all three nanostructure arrays showed photocatalytic activities under visible light, their degradation pathway are found to be different. The least effective dye-sensitization mechanism is responsible for the RhB degradation in the presence of ZnO nanowire arrays, while the highly-reactive radicals produced by photogenerated electron-hole pairs in visible-light-excited ZnFe₂O₄ contributes to RhB degradation in both ZnO/ZnFe₂O₄ nanocable arrays and ZnFe₂O₄ nanotube arrays. The type II band alignment between ZnO and ZnFe₂O₄ leads to effective charge carrier separation in the nanocable arrays, but is absent in the case of ZnFe₂O₄ nanotube arrays. This explains the more efficient RhB decomposition in the presence of the ZnO-core/ZnFe₂O₄-shell nanocable arrays.

© 2014 Elsevier B.V. All rights reserved.

1. Introduction

In recent years, great efforts have been devoted to the development of the semiconductor-based photocatalysis for water and air purification, addressing the increasing problem of environmental pollution worldwide. Among various semiconductor-based photocatalysts, zinc oxide (ZnO) has received considerable attention due to its good photocatalytic activity [1–5]. However, its large bandgap (~3.2 eV) only allows it absorbing UV light for the required band gap excitation and charge carrier generation, limiting its light harvesting efficiency, since UV light only contributes ~4% of the solar energy [6]. In fact, visible light contributes about 50% of the solar energy. This makes the visible-light-driven photocatalysts promising for practical applications. Although ZnO can utilize the visible range of solar spectrum via a dye-sensitization mechanism, but the corresponding efficiency remains low [7,8]. Alternative solution is to directly use semiconductors with smaller band gap. For example, zinc ferrite (ZnFe₂O₄) has a bandgap of ~2.3 eV [9,10], matching the visible range of solar spectrum. However, due to the rapid recombination of photogenerated electrons and holes, ZnFe₂O₄ itself usually shows rather poor photogradation activities [11–13]. Generally speaking, the performance of the visible-light-driven photocatalysts made of single-component semiconductor is not

satisfactory to date [14]. One of the promising solutions is coupling two different semiconductors forming a heterojunction. The behaviors of electrons and holes at the heterojunction interface depend on the band alignment of the two semiconductors. If the conduction band minimum (CBM) of one semiconductor is more positive than that of the other, while the valence band maximum (VBM) of the former is more negative than that of the latter, they form a type I heterojunction. Both electrons and holes are driven to the narrower-bandgap semiconductor due to the internal electric field and recombine with each other efficiently. Such heterojunctions are commonly used in light emitting applications. On the other hand, if both CBM and VBM of one semiconductor are more positive (or negative) than that of the other, a type II band alignment forms. The electrons and holes can be driven to opposite directions and physically separated, thus minimizing their recombination. This configuration is often employed in photovoltaic and photocatalytic applications [15,16]. A number of semiconductor combinations have been identified to have type II alignment. The band gap energies of these semiconductors and their band alignments have been summarized in recent literatures [17–19]. Practically, semiconductor heterojunctions with type II band alignment, such as TiO₂/CdS [20–22], TiO₂/WO₃ [23], TiO₂/ZnFe₂O₄ [24,25], ZnO/CdS [26], ZnO/Zn₂TiO₄ [27], have shown good photocatalytic activities.

Among various morphologies, pseudo-one-dimensional (pseudo-1D) nanostructures (e.g., nanowires, nanobelts, nanotubes, nanocables, etc.) are promising structures for photocatalytic applications—the 1D morphology is ideal for efficient transport of

* Corresponding author. Tel.: +852 39436323.
E-mail address: liquan@phy.cuhk.edu.hk (Q. Li).

electrons. Moreover, when these nanostructures are fabricated on a substrate in an aligned manner, they may enhance light absorption [28–31]. In addition, some of them can serve as templates for the growth of other pseudo-1D materials, making it possible to form desired heterojunctions.

Binary-compound pseudo-1D nanostructures (e.g., ZnO nanowires) are widely studied and can be synthesized using both vapor-based methods and solution-based methods [32–38]. Among various 1D nanostructures, ZnO is probably one of the easiest to grow into 1D morphology in the absence of any catalyst. This is due to the crystalline anisotropy of ZnO—the polar {0001} planes have higher surface energy than other common-observed nonpolar planes (e.g., {0110}, {2110}) in most cases, so that the growth rate along [0001] direction becomes the highest [33,35,39]. However, obtaining ternary-compound pseudo-1D nanostructures is more complicated. Multi-step recipes or multiple precursors are often involved [40–44]. For example, ZnFe₂O₄ nanorods can be obtained via microemulsion method [45,46] and/or electrospun method followed by annealing [47]. ZnFe₂O₄ nanotubes can be fabricated via sol-gel method or electrochemical method with the help of anodic aluminum oxide (AAO) membrane to confine the 1D growth [46,48–51]. It is also possible to synthesize ZnFe₂O₄ nanotubes via the solid reactions between ZnO and iron oxides at elevated temperatures [10,52]. The synthesis of semiconductor heterojunction at nanoscale (e.g., core/shell nanocables) is even more difficult and rather limited comparing to single-component nanostructures. For core/shell nanocables, the core nanowires are usually fabricated in first step and then the shell material is coated on the surface of the core preventing the damage of its morphology and composition. Successful examples include ZnO/ZnFe₂O₄ nanocables [40], ZnO/CdSe nanocable arrays [53], ZnO/ZnSe nanocable arrays [54], ZnO/Zn_xCd_{1-x}Se nanocable arrays [55], ZnO/CdTe nanocable arrays [56], CdS/Cu_xS nanocables [57], Si/InGaN core/shell hierarchical nanowire arrays [58], etc.

In the present work, the ZnO-core/ZnFe₂O₄-shell nanocable with aligned array configuration is successfully obtained by a simple sacrificial ZnO-nanowire-array templating method. Similar to other pseudo-1D nanostructures, the nanocable array configuration associated with large surface-to-volume ratio, leading to optical path increase of the incident light in the structure and suppress reflection, and thus enhanced light absorption [28–31]. More importantly, by forming a type II band alignment between ZnO core and the ZnFe₂O₄-shell, one should expect improved charge carrier separation and thus enhance photocatalytic activity. The photocatalytic properties of the nanocable arrays were compared to those obtained from pure ZnO and ZnFe₂O₄ nanotube arrays, and their respective photocatalytic mechanisms are discussed in detail.

2. Experimental

The three kinds of pseudo-1D Zn–Fe–O nanostructures (i.e., ZnO nanowire arrays, ZnO/ZnFe₂O₄ core/shell nanocable arrays and ZnFe₂O₄ nanotube arrays) were synthesized on three single-crystalline sapphire substrates (approximately 1 cm × 1 cm, labeled S1, S2 and S3), respectively. The scheme of the synthesis processes is shown in Fig. 1 and the detailed growth procedures can be found elsewhere [10]. Briefly, three identical substrates were firstly bonded onto one piece of glass slide and hydrothermal ZnO-nanowire-array growth was carried out on these substrates. Secondly, S1 was removed from the glass slide for further treatment. S2 and S3 were simultaneously immersed into 0.05 M FeCl₃ aqueous solution with vigorous shaking for 10 s and rinsed with DI water. Next, S1, S2 and S3 were calcined in the air for 5 h at 700 °C together. This leads to the formation of the nanocable arrays on S2 and S3. Then, the calcined ZnO-nanowire-array on the S1 is labeled

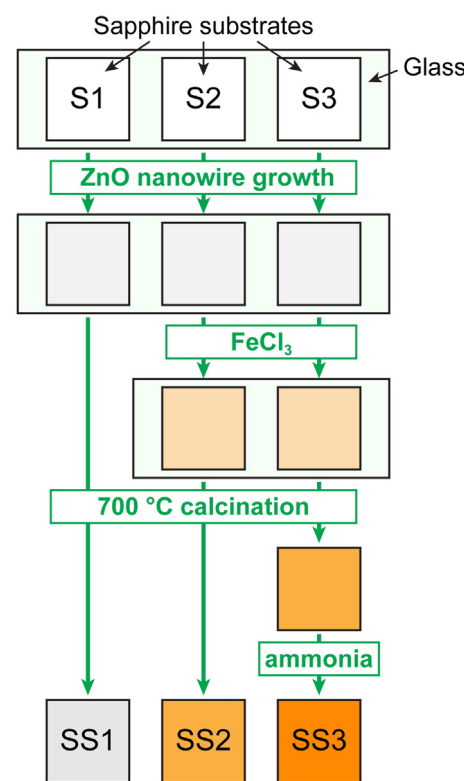


Fig. 1. The synthesis processes of three pseudo-1D Zn–Fe–O nanostructures on sapphire substrates.

SS1, and nanocable arrays aligned on the S2 is labeled SS2. Finally, the excess ZnO core on S3 was removed by 25% NH₃ solution for 24 h, forming nanotube arrays (labeled SS3).

The general morphology of the three pseudo-1D nanostructure arrays on sapphire substrates was characterized using scanning electron microscopy (SEM; Quantum F400) and their crystallinity were examined by X-ray diffraction (XRD) using a diffractometer with Cu K α radiation (Rigaku SMARTLAB XRD). The detailed microstructures and chemical compositions were investigated using transmission electron microscopy or scanning transmission electron microscopy (TEM/STEM; Tecnai Spirit 12 and Tecnai 20 FEG) equipped with an energy-dispersive X-ray spectrometer (EDX). The visible-light photocatalytic activities of the samples (~1 cm × 1 cm) were evaluated from the degradation of 10 ppm rhodamine B (RhB) aqueous solution with or without 1 M CH₃OH as the hole scavenger. The photodegradation reaction was performed in a 5 ml special home-made photoreactor, which was cooled by the circulating water and capped by a piece of quartz. After the adsorption–desorption equilibrium between the RhB solution and the photocatalyst was reached in dark under magnetic stirring, the photodegradation experiment was started by illuminating the photoreactor with the visible light. The illumination source was a 150 W Xenon lamp (Bentham IL7) equipped with a 400 nm long-pass filter. The degradation process was monitored by measuring the absorption spectra of the RhB solutions using Hitachi U3501 spectrophotometer every 1 h.

3. Results and discussion

3.1. Morphologies, crystal structures and chemical compositions

The three batches of samples were made in a parallel manner, so that their density on the substrate is similar. Fig. 2 illustrates the morphology evolution of Zn–Fe–O pseudo-1D nanostructure

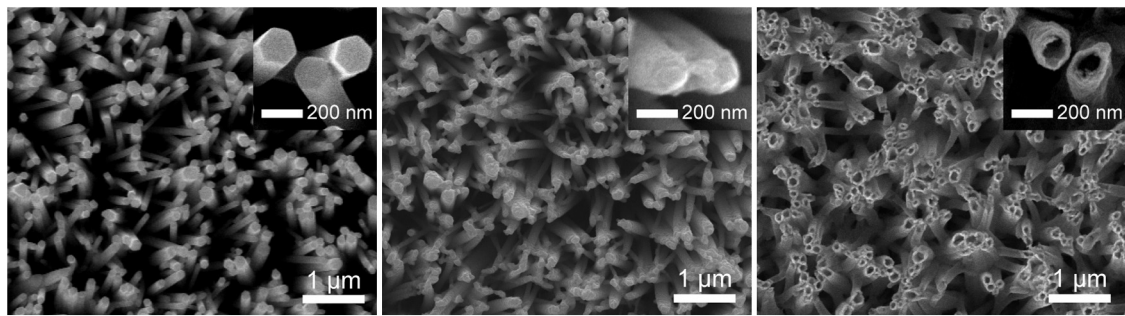


Fig. 2. SEM images of (a) SS1, (b) SS2, and (c) SS3. The insert in each image shows the corresponding SEM image at larger magnification.

arrays, that is, from ZnO nanowires to ZnO/ZnFe₂O₄ core/shell nanocables and to ZnFe₂O₄ nanotubes. Sample SS1 (700 °C calcinated ZnO nanowire arrays) are vertically aligned on the sapphire substrate (Fig. 2(a)). Each nanowire on the substrate has well-defined hexagonal cross section and smooth surface. Their diameters are around 200 nm. After treatment of FeCl₃ solution and calcination, the surface of the nanowires becomes rough, forming a core/shell structure (i.e., sample SS2). Then, etching the ZnO cores away leads to the formation of nanotube arrays (i.e., sample SS3). The inner diameters of nanotubes are around 150 nm and the wall thicknesses are about 50 nm.

The crystalline structures of the three pseudo-1D nanostructure arrays on sapphire were studied by XRD (Fig. 3). The diffraction peaks from the sapphire substrates are marked with asterisks. For sample SS1 (Fig. 3(b)), all the diffraction peaks can be indexed to those of ZnO wurtzite structure (JCPDS Card No. 36-1451). For sample SS2, besides the diffraction peaks from wurtzite ZnO, the remaining peaks (Fig. 3(c)) can be assigned to cubic spinel structure of ZnFe₂O₄ (JCPDS No. 89-7412). After removal of ZnO cores, all of the diffraction peaks from ZnO disappear, leaving those characteristic of ZnFe₂O₄ only, as shown in the XRD spectrum of sample SS3 (Fig. 3(d)).

TEM-related techniques are used to examine the change of microstructures and compositions during the nanostructure formation in a detailed manner. The original ZnO nanowire is observed to have a smooth surface from the TEM image (Fig. 4(a)). Selected-area diffraction (SAD) pattern (Fig. 4(b)), taken from a single nanowire, reveals its single crystalline nature. The corresponding energy-dispersive X-ray (EDX) spectrum (Fig. 4(c)) only shows signals from

Zn and O with the atomic ratio between Zn and O close to 1 (the Cu signals in all of the EDX spectra comes from the TEM supporting grid).

After FeCl₃ immersion and calcination, the surface of the ZnO nanowire becomes rough and is covered with a thin shell (Fig. 5(a)). Besides the diffraction spots from wurtzite ZnO, the SAD patterns also show ring patterns, which can be indexed to cubic ZnFe₂O₄ (Fig. 5(b)). The ring patterns also indicate the polycrystalline nature of ZnFe₂O₄ shell. Moreover, the signals from Fe also appear in the EDX spectrum of sample SS2 and the atomic ratio of Zn:O also deviate from 1, due to the formation of ZnFe₂O₄ outside ZnO (Fig. 5(b)). In order to recognize the ZnFe₂O₄ nanoshell clearly, the STEM-EDX mapping is carried out from one of the nanocables, disclosing the spatial distribution of the compositional elements (i.e., Zn, Fe and O). The results (Fig. 5(d)) show that the Zn and O signals present throughout the whole nanocable, while the intensity of Fe is mainly confined in the shell regions, suggesting the ZnO-core/ZnFe₂O₄-shell configuration of the nanocable.

The etching of ZnO core leads to the formation of the pure ZnFe₂O₄ nanotubes (Fig. 6(a)). The SAD pattern of such nanotube only exhibits one set of ring pattern, which can be indexed to polycrystalline cubic ZnFe₂O₄ (Fig. 6(b)). The atomic ratios of Zn:Fe:O, as revealed by the corresponding EDX spectrum (Fig. 6(c)), are close to 1:2:4. The STEM-EDX mapping of a single nanotube (Fig. 6(d)) shows similar spatial distribution of all the three elements (i.e., Zn, Fe and O), suggesting the nanotube configuration.

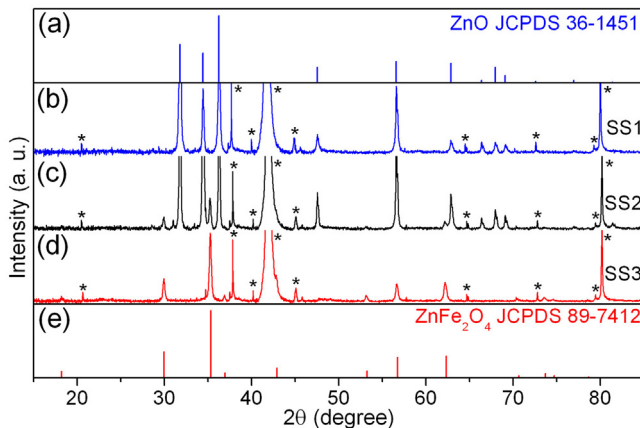


Fig. 3. XRD spectra of (b) SS1, (c) SS2, and (d) SS3, together with the standard XRD data of (a) ZnO and (e) ZnFe₂O₄. The diffraction peaks marked with asterisks come from the sapphire substrates and the strong peaks are cut off in order to show all small peaks clearly.

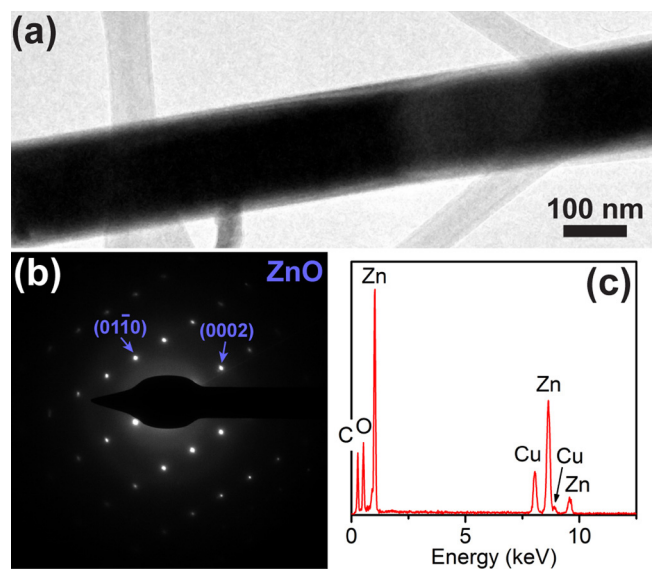


Fig. 4. (a) TEM image of sample SS1 and corresponding (b) SAD pattern and (c) EDX spectrum taken from the same sample.

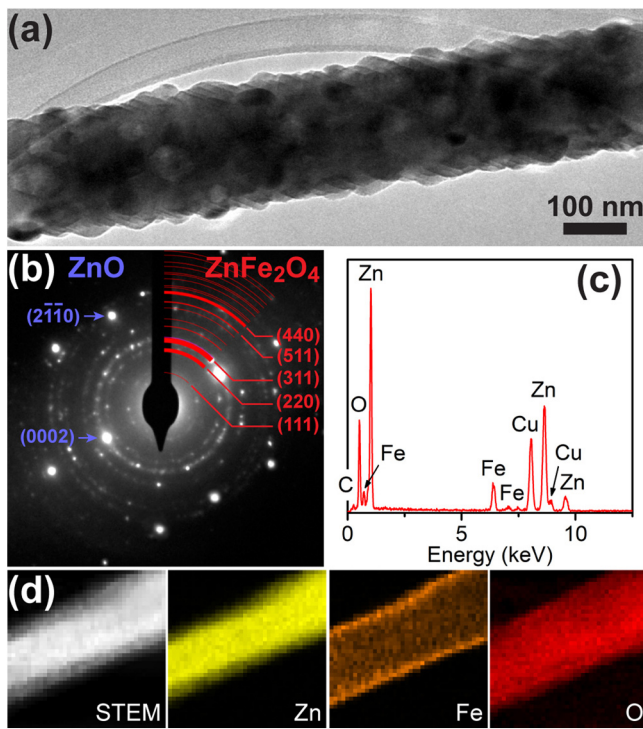


Fig. 5. (a) TEM image of sample SS2 and corresponding (b) SAD pattern and (c) EDX spectrum taken from the same sample. (d) The elemental mapping extracted from STEM-EDX showing the spatial distribution of the compositional elements (Zn, Fe and O) of the nanocable.

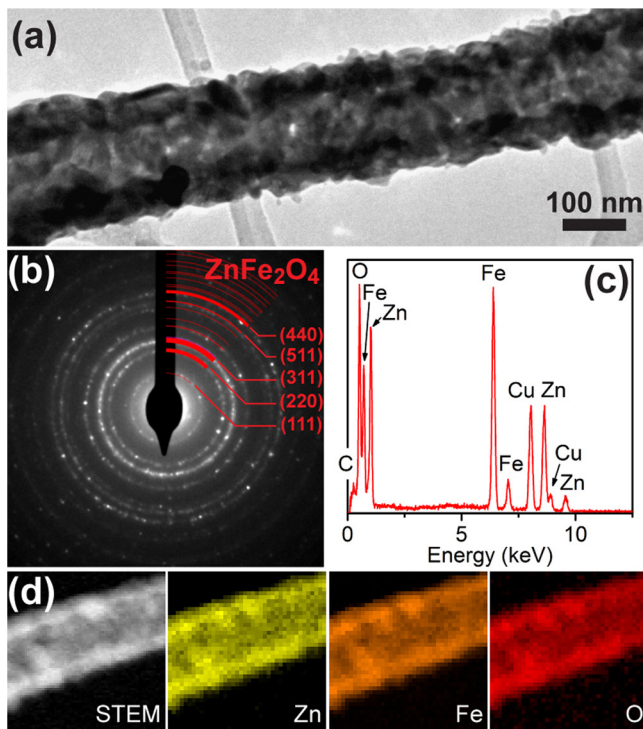


Fig. 6. (a) TEM image of sample SS3 and corresponding (b) SAD pattern and (c) EDX spectrum taken from the same sample. (d) The elemental mapping extracted from STEM-EDX showing the spatial distribution of the compositional elements (Zn, Fe and O) of the nanotube.

3.2. Photocatalytic activities

The photocatalytic activities of the three pseudo-1D nanostructure arrays under visible light ($\lambda > 400$ nm) are investigated using the degradation of RhB as the probe reaction. In the blank experiment, no photocatalyst is used. The major absorption peak of RhB at 553 nm only shows a very small decrease of ~5% after 3 h and the peak center remains unchanged (Fig. 7(a)). Such decrease can be attributed to the direct photolysis of RhB molecules under visible light irradiation. In the presence of ZnO nanowire arrays, 29% RhB molecules are decolorized after 3 hours' irradiation. The peak maximum slightly shifts from 553 nm to 549 nm (Fig. 7(b)). After coating the ZnO nanowires with visible-light-active ZnFe₂O₄ crystals, the photodegradation performance is greatly enhanced. The absorption peak of the dye solution dramatically dropped to 11% of its initial height (i.e., 89% RhB is decolorized) and the peak center also exhibits a large blue shift from 553 nm to 498 nm (Fig. 7(c)) after 3 hours' irradiation. However, when removing the ZnO cores from the nanocables, the photocatalytic activities are worsened. As shown in Fig. 7(d), the absorbance only decreases by 43% after 3 hour's illumination and the amount of peak shift also becomes smaller (from 553 nm to 542 nm) than that of the nanocable sample.

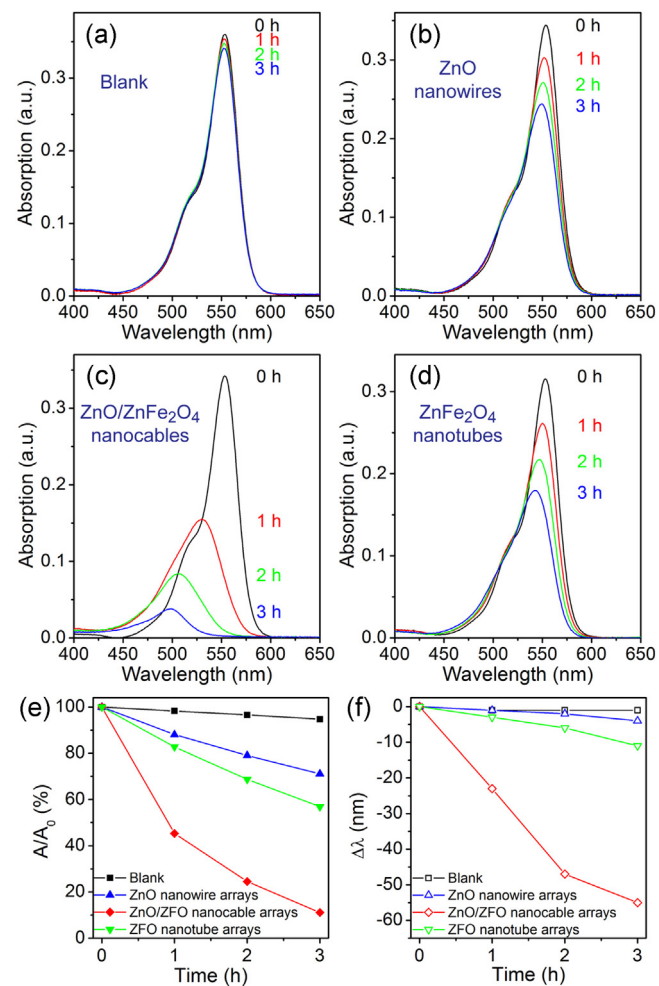
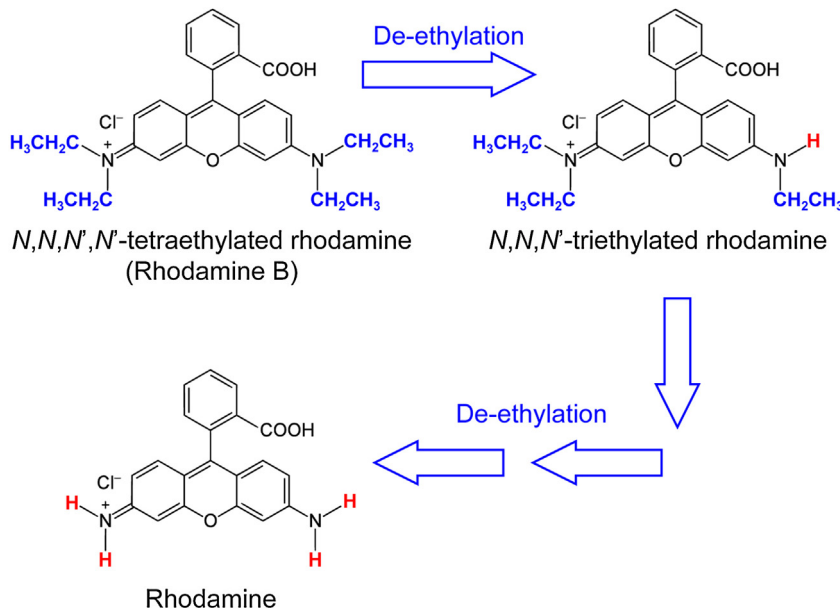


Fig. 7. The change of the absorption spectra of RhB aqueous solutions (10 ppm) with irradiation time under visible light ($\lambda > 400$ nm) (a) without any photocatalysts, at the presence of (b) ZnO nanowire arrays, (c) ZnO/ZnFe₂O₄ nanocable arrays and (d) ZnFe₂O₄ nanotube arrays on sapphire substrates. The summary of the RhB absorption spectra change as a function of illumination time, including (e) absorbance (A/A_0) decrease and (f) peak position ($\Delta\lambda$) shift.

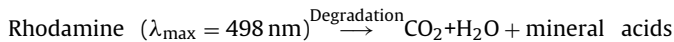
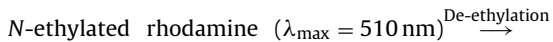
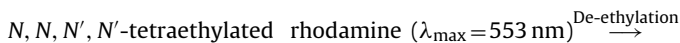
**Fig. 8.** Step-by-step de-ethylation of rhodamine B.

The degradation performance of the three nano photocatalysts, considering both the RhB absorbance decrease and peak position shift, are summarized and compared in Fig. 7(e) and (f). Since the degradation reaction of RhB can be described as a pseudo-first-order reaction, the degradation reaction rate k of the three photocatalysts can be estimated by the following equation when the dye concentration is low (<1 mM),

$$\ln \frac{C_0}{C} = kt \quad (1)$$

where C_0 is the initial concentration of RhB and C is the RhB concentration at time t [59]. The calculated reaction rate constant k of ZnO nanowire arrays, ZnO/ZnFe₂O₄ nanocable arrays and ZnFe₂O₄ nanotube arrays are estimated as $\sim 1.2 \times 10^{-3}$ min⁻¹, $\sim 1.2 \times 10^{-2}$ min⁻¹ and $\sim 3.1 \times 10^{-3}$ min⁻¹, respectively.

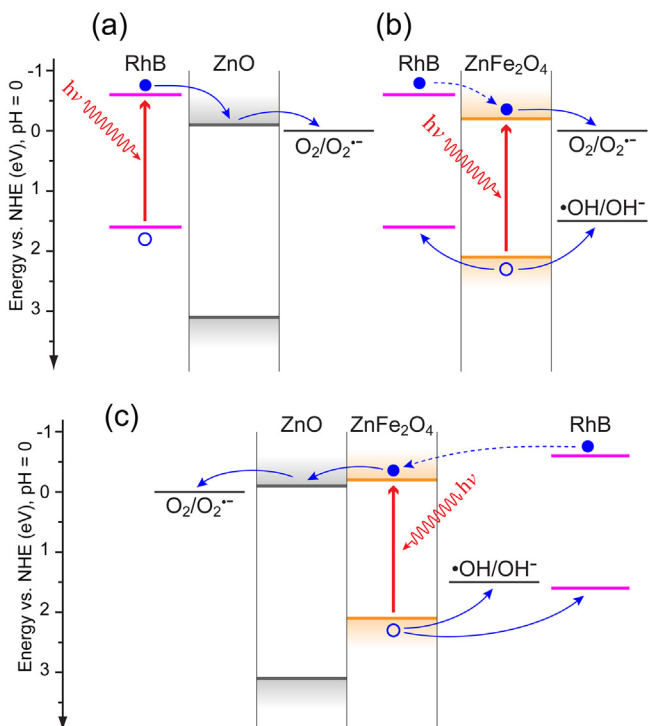
Generally speaking, RhB molecules usually have two different degradation pathways, including the de-ethylation and the degradation of chromophore processes [60–67]. The degradation of chromophore of RhB involves the decomposition reaction of its conjugated ring structure, which is responsible for the color of the molecule, but will not cause an absorption peak shift. On the other hand, the de-ethylation of RhB molecule (i.e., the fully *N,N,N',N'*-tetraethylated rhodamine) takes place following the equations below [68–70],



The four ethyl groups are removed one by one until RhB is completely converted to rhodamine with no ethyl group (Fig. 8), leading to a large blue shift of the RhB absorption peak from 553 nm to 498 nm. After that, the conjugated ring structure of rhodamine is

destroyed, resulting in further decrease of the absorption peak but without peak shift.

Although the bandgap of ZnO (~3.2 eV) is larger than the energy of the incident visible light, the degradation of RhB is also observed at the existence of ZnO nanowire arrays under visible light irradiation, which can be attributed to the dye-sensitized mechanism [71]. As shown in energy diagram of ZnO (Fig. 9(a)), its CBM (−0.1 V vs. NHE) [72–75] is more positive than lowest

**Fig. 9.** The schematic diagrams showing the different degradation mechanisms of RhB by (a) ZnO nanowire arrays, (b) ZnFe₂O₄ nanotube arrays and (c) ZnO/ZnFe₂O₄ nanocable arrays in 10 ppm RhB aqueous solutions under visible light ($\lambda > 400$ nm) illumination for 3 hours, after the adsorption–desorption equilibrium between the RhB solution and the photocatalyst was reached in dark under magnetic stirring.

unoccupied molecular orbital (LUMO) of RhB (-0.6 V vs. NHE) [32], but more negative than the reduce potential of water-dissolved O_2 , $E(O_2/O_2^{*-})$ (0.0 V vs. NHE [15,76]). When irradiated with visible light, electron–hole pairs cannot be generated in ZnO directly. However, the RhB molecules can be excited to the excited states and inject electrons to CBM of ZnO. Then, these electrons are captured by the O_2 in water, producing superoxide radicals O_2^{*-} . These radicals further lead to chromophore degradation of RhB molecules [64,66], showing peak intensity decrease in RhB absorption spectra with subtle shift in the peak position. However, the overall degradation efficiency via this route is low (29% degradation after 3 hours' illumination).

As a narrow bandgap semiconductor, $ZnFe_2O_4$ has the ability to utilize the visible light. The CBM of $ZnFe_2O_4$ (-0.2 V vs. NHE) [77] is more negative than $E(O_2/O_2^{*-})$ and its VBM (2.1 V vs. NHE) [77] is more positive than the oxidation potential of OH group $E(\cdot OH/OH^-)$ (1.5 V vs. NHE) [73,78] and highest occupied molecular orbital (HOMO) of RhB (1.6 V vs. NHE) [76] (Fig. 9(b)). Thus, upon illumination, electron–hole pairs are generated in $ZnFe_2O_4$ nanotubes. The electrons are captured by O_2 , forming O_2^{*-} radicals, leading to degradation of chromophore of RhB. The holes in the VBM of $ZnFe_2O_4$ directly oxidize RhB or react with the surface-adsorbed OH group forming $\cdot OH$ radicals. These active pieces prior cause de-ethylation of RhB molecules, resulting in a large blue shift in the peak positions [60,61,64,66,69]. Combining the effects of both electrons and holes, $ZnFe_2O_4$ nanotube arrays shows not only absorbance decrease, but also peak shift after 3 hours' irradiation. However, the photocatalytic activity is still low (~43% absorption drop), due to the lacking of an efficient charge carrier separation mechanism. The photogenerated electron–holes cannot be effectively used before their possible recombination.

When the ZnO and $ZnFe_2O_4$ are coupled together, forming ZnO/ $ZnFe_2O_4$ core/shell nanocable arrays, a type II band alignment is formed between the two, i.e., both the CBM and VBM of $ZnFe_2O_4$ are more negative than those of ZnO (Fig. 9(c)). Consequently, the photogenerated electron–hole pairs in $ZnFe_2O_4$ shells can be separated efficiently. The electrons are driven to CBM of ZnO and the holes are left in the VBM of $ZnFe_2O_4$. Both electrons and holes can contribute to the photodegradation processes, thus leading to large absorbance decrease (~89% drop) and obvious peak shift (-55 nm) after 3 hours' irradiation.

As discussed above, both electrons and holes can attribute to the degradation process but take different degradation pathways. Electrons mainly contribute to the degradation of chromophore and holes mainly contribute to de-ethylation process. Further evidence is provided by adding CH_3OH , which is a typical hole scavenger in aqueous solution [79,80]. Little change is observed in the blank experiment (in the absence of any photocatalyst) after adding CH_3OH (Fig. 10(a)). However, the three nanostructures show different behaviors. For ZnO nanowire arrays, its photocatalytic activity is almost unchanged (Fig. 10(b)) in the presence of hole scavenger. Although the presence of hole scavenger supposes to suppress the charge carrier recombination, and thus contribute to longer electron life time, it does not help to improve the photocatalytic activity of the ZnO nanowire arrays. This result confirms that the photodegradation of ZnO nanowires mainly relies on electron-involved pathways, and suggests that the rate-limiting step for ZnO photo-catalytic reaction could be electron transfer from RhB to ZnO.

However, for ZnO/ $ZnFe_2O_4$ core/shell nanocable arrays, the absorbance decrease of RhB becomes much smaller and the peak maximum shift becomes negligible, as compared results obtained in the absence of CH_3OH (Fig. 10(c)). Since both electrons and holes contribute to the degradation process in the nanocable arrays, once a large amount of holes are scavenged, only electron-involved pathways contribute to the photodegradation process. This explains

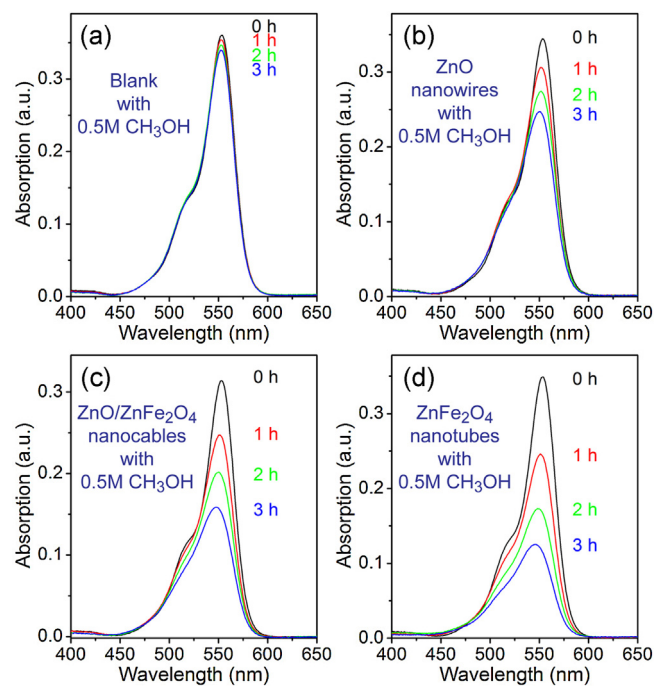


Fig. 10. Evolution of the absorption spectra of RhB aqueous solutions (10 ppm RhB, adding 1 M CH_3OH) under visible light ($\lambda > 400$ nm) as a function of the irradiation duration (a) in the absence of any photocatalysts; in the presence of (b) ZnO nanowire arrays; (c) ZnO/ $ZnFe_2O_4$ nanocable arrays; and (d) $ZnFe_2O_4$ nanotube arrays on sapphire substrates.

both the weakened photodegradation capability of the nanocables and the disappearances of RhB absorption peak shifting along with its intensity decrease.

On the contrary, the $ZnFe_2O_4$ nanotube arrays show improved photocatalytic activity and little peak shift is observed after 3 hours' illumination in the presence of CH_3OH . This may be attributed to the reduced charge carrier recombination, and thus longer electron life time, due to the consumption of holes by the hole scavenger. Although the contribution of holes to photo degradation is much weakened, the increase in contribution by electron-involved pathways may exceed that of the holes, resulting in an improved photocatalytic activity.

4. Conclusions

In conclusion, the visible-light-driven photodegradation activities of ZnO/ $ZnFe_2O_4$ nanocable arrays were demonstrated to be superior to those of the ZnO nanowire arrays and $ZnFe_2O_4$ nanotube arrays. Although all three nanostructure arrays show degradation of RhB under visible light illumination, their degradation pathways were found to be different. The degradation of RhB in the presence of ZnO nanowire arrays is attributed to the dye-sensitized mechanism (which is the least effective one), while in the case of $ZnFe_2O_4$ nanotube arrays, the production of reactive radicals by the photogenerated electron–hole pairs in the visible-light-active $ZnFe_2O_4$ are mainly responsible for the photodegradation of RhB. The nanocable arrays shares the same degradation mechanism as the pure $ZnFe_2O_4$ nanotube arrays, but exhibiting a much higher degradation efficiency. This is due to effective separation of the photogenerated electron–hole pairs in $ZnFe_2O_4$, as driven by the type II band alignment between ZnO and $ZnFe_2O_4$. In addition, the nanocables can be obtained via a scalable wet chemistry process. Moreover, the array-on-substrate configuration makes them very convenient to be recycled after use comparing to their

freestanding counterparts. These characteristics make them promising candidate for a wide range photocatalytic applications.

Acknowledgements

The work described in this paper was substantially supported by a grant from the Research Grants Council of the Hong Kong Special Administrative Region, China, under Theme-based Research Scheme through Project No. T23-407/13-N.

References

- [1] C.G. Tian, Q. Zhang, A.P. Wu, M.J. Jiang, Z.L. Liang, B.J. Jiang, H.G. Fu, *Chem. Commun.* 48 (2012) 2858–2860.
- [2] E.S. Jang, J.H. Won, S.J. Hwang, J.H. Choy, *Adv. Mater.* 18 (2006) 3309–3312.
- [3] B.X. Li, Y.F. Wang, *J. Phys. Chem. C* 114 (2010) 890–896.
- [4] F. Lu, W.P. Cai, Y.G. Zhang, *Adv. Funct. Mater.* 18 (2008) 1047–1056.
- [5] A. McLaren, T. Valdes-Solis, G.Q. Li, S.C. Tsang, *J. Am. Chem. Soc.* 131 (2009) 12540–12541.
- [6] ASTM G173-03 Reference Spectra.
- [7] C.S. Lu, Y.T. Wu, F.D. Mai, W.S. Chung, C.W. Wu, W.Y. Lin, C.C. Chen, *J. Mol. Catal. a-Chem.* 310 (2009) 159–165.
- [8] B. Pare, S.B. Jonnalagadda, H. Tomar, P. Singh, V.W. Bhagwat, *Desalination* 232 (2008) 80–90.
- [9] A.A. Tahir, K.G.U. Wijayantha, M. Mazhar, V. McKee, *Thin Solid Films* 518 (2010) 3664–3668.
- [10] X. Guo, H. Zhu, M. Si, C. Jiang, D. Xue, Q. Li, *CrystEngComm* 15 (2013) 8306–8313.
- [11] C.H. Chen, Y.H. Liang, W.D. Zhang, *J. Alloy. Compd.* 501 (2010) 168–172.
- [12] X.B. Cao, L. Gu, X.M. Lan, C. Zhao, D. Yao, W.J. Sheng, *Mater. Chem. Phys.* 106 (2007) 175–180.
- [13] S.H. Xu, D.L. Feng, W.F. Shangguan, *J. Phys. Chem. C* 113 (2009) 2463–2467.
- [14] H. Zhu, Q. Li, *Nanoscale Res. Lett.* 8 (2013) 1–6.
- [15] H.J. Zhang, G.H. Chen, D.W. Bahnemann, *J. Mater. Chem.* 19 (2009) 5089–5121.
- [16] A.I. Hochbaum, P. Yang, *Chem. Rev.* 110 (2009) 527–546.
- [17] W. Walukiewicz, *Phys. B: Cond. Matter* 302 (2001) 123–134.
- [18] C.G. van de Walle, J. Neugebauer, *Nature* 423 (2003) 626–628.
- [19] T. Bak, J. Nowotny, M. Rekas, C. Sorrell, *Int. J. Hydrogen Energy* 27 (2002) 991–1022.
- [20] S. Liu, N. Zhang, Z.-R. Tang, Y.-J. Xu, *ACS Appl. Mater. Interfaces* 4 (2012) 6378–6385.
- [21] G.-S. Li, D.-Q. Zhang, J.C. Yu, *Environ. Sci. Technol.* 43 (2009) 7079–7085.
- [22] Y. Bessekhouad, D. Robert, J. Weber, *J. Photochem. Photobiol. A Chem.* 163 (2004) 569–580.
- [23] S. Higashimoto, M. Sakiyama, M. Azuma, *Thin Solid Films* 503 (2006) 201–206.
- [24] Y. Hou, X. Li, Q. Zhao, X. Quan, G. Chen, *Adv. Funct. Mater.* 20 (2010) 2165–2174.
- [25] X. Li, Y. Hou, Q. Zhao, G. Chen, *Langmuir* 27 (2011) 3113–3120.
- [26] Y. Tak, H. Kim, D. Lee, K. Yong, *Chem. Commun.* (2008) 4585–4587.
- [27] L. Wan, X. Li, Z. Qu, Y. Shi, H. Li, Q. Zhao, G. Chen, *J. Hazard. Mater.* 184 (2010) 864–868.
- [28] J. Zhu, Z.F. Yu, G.F. Burkhard, C.M. Hsu, S.T. Connor, Y.Q. Xu, Q. Wang, M. McGehee, S.H. Fan, Y. Cui, *Nano Lett.* 9 (2009) 279–282.
- [29] E. Garnett, P. Yang, *Nano Lett.* 10 (2010) 1082–1087.
- [30] L. Yu, S. Misra, J. Wang, S. Qian, M. Foldyna, J. Xu, Y. Shi, E. Johnson, P.R.J. Cabarreras, *Sci. Rep.* 4 (2014).
- [31] L. Hu, G. Chen, *Nano Lett.* 7 (2007) 3249–3252.
- [32] M. Law, J. Goldberger, P.D. Yang, *Ann. Rev. Mater. Res.* 34 (2004) 83–122.
- [33] Z.L. Wang, *J. Phys.-Cond. Matter* 16 (2004) R829–R858.
- [34] L. Schmidt-Mende, J.L. MacManus-Driscoll, *Mater. Today* 10 (2007) 40–48.
- [35] Z.L. Wang, *Mater. Sci. Eng. R-Rep.* 64 (2009) 33–71.
- [36] C. Klingshirn, J. Fallert, H. Zhou, J. Sartor, C. Thiele, F. Maier-Flaig, D. Schneider, H. Kalt, *Phys. Status Solidi B-Basic Solid State Phys.* 247 (2010) 1424–1447.
- [37] B. Weintraub, Z.Z. Zhou, Y.H. Li, Y.L. Deng, *Nanoscale* 2 (2010) 1573–1587.
- [38] S. Xu, Z.L. Wang, *Nano Res.* 4 (2011) 1013–1098.
- [39] X.Y. Kong, Z.L. Wang, *Appl. Phys. Lett.* 84 (2004) 975–977.
- [40] H.J. Fan, Y. Yang, M. Zacharias, *J. Mater. Chem.* 19 (2009) 885–900.
- [41] J. Xu, C.Y. Luan, Y.B. Tang, X. Chen, J.A. Zapien, W.J. Zhang, H.L. Kwong, X.M. Meng, S.T. Lee, C.S. Lee, *ACS Nano* 4 (2010) 6064–6070.
- [42] A. Kok, Z. Zhou, H.A. Sodano, *Energy Environ. Sci.* 7 (2014) 288–296.
- [43] D.T. Schoen, H. Peng, Y. Cui, *ACS Nano* 7 (2013) 3205–3211.
- [44] H.J. Fan, M. Knez, R. Scholz, K. Nielsch, E. Pipppel, D. Hesse, M. Zacharias, U. Gosele, *Nat. Mater.* 5 (2006) 627–631.
- [45] H. Zhu, X. Gu, D. Zuo, Z. Wang, N. Wang, K. Yao, *Nanotechnology* 19 (2008) 405503.
- [46] S. Liu, B. Yue, K. Jiao, Y. Zhou, H. He, *Mater. Lett.* 60 (2006) 154–158.
- [47] P.F. Teh, Y. Sharma, S.S. Pramana, M. Srinivasan, *J. Mater. Chem.* 21 (2011) 14999–15008.
- [48] X. Li, Y. Hou, Q. Zhao, W. Teng, X. Hu, G. Chen, *Chemosphere* 82 (2011) 581–586.
- [49] F. Liu, X. Li, Q. Zhao, Y. Hou, X. Quan, G. Chen, *Acta Mater.* 57 (2009) 2684–2690.
- [50] J.-S. Jung, Y.-K. Jung, E.-M. Kim, S.-H. Min, J.-H. Jun, L.M. Malkinski, Y. Barnakov, L. Spinu, K. Stokes, *Trans IEEE Magnetics* 41 (2005) 3403–3405.
- [51] D. Gao, Z. Shi, Y. Xu, J. Zhang, G. Yang, J. Zhang, X. Wang, D. Xue, *Nanoscale Res. Lett.* 5 (2010) 1289–1294.
- [52] M. Mo, T. Ma, L. Jia, L. Peng, X. Guo, W. Ding, *Mater. Lett.* 63 (2009) 2233–2235.
- [53] M.J. Zhou, H.J. Zhu, X.N. Wang, Y.M. Xu, Y. Tao, S. Hark, X.D. Xiao, Q. Li, *Chem. Mater.* 22 (2010) 64–69.
- [54] K. Wang, J.J. Chen, W.L. Zhou, Y. Zhang, Y.F. Yan, J. Pern, A. Mascarenhas, *Adv. Mater.* 20 (2008) 3248–+.
- [55] J. Xu, X. Yang, H. Wang, X. Chen, C. Luan, Z. Xu, Z. Lu, V.A.L. Roy, W. Zhang, C.-S. Lee, *Nano Lett.* 11 (2011) 4138–4143.
- [56] X.N. Wang, H.J. Zhu, Y.M. Xu, H. Wang, Y. Tao, S. Hark, X.D. Xiao, Q.A. Li, *ACS Nano* 4 (2010) 3302–3308.
- [57] J. Tang, Z. Huo, S. Britzman, H. Gao, P. Yang, *Nat. Nanotechnol.* 6 (2011) 568–572.
- [58] Y.J. Hwang, C.H. Wu, C. Hahn, H.E. Jeong, P. Yang, *Nano Lett.* 12 (2012) 1678–1682.
- [59] D.F. Ollis, *Environ. Sci. Technol.* 19 (1985) 480–484.
- [60] Y. Ma, J.N. Yao, *J. Photochem. Photobiol. a-Chem.* 116 (1998) 167–170.
- [61] Q. Wang, C.C. Chen, D. Zhao, W.H. Ma, J.C. Zhao, *Langmuir* 24 (2008) 7338–7345.
- [62] J.D. Zhuang, W.X. Dai, Q.F. Tian, Z.H. Li, L.Y. Xie, J.X. Wang, P. Liu, X.C. Shi, D.H. Wang, *Langmuir* 26 (2010) 9686–9694.
- [63] Z.X. Chen, D.Z. Li, W.J. Zhang, Y. Shao, T.W. Chen, M. Sun, X.Z. Fu, *J. Phys. Chem. C* 113 (2009) 4433–4440.
- [64] J. Yang, C.C. Chen, H.W. Ji, W.H. Ma, J.C. Zhao, *J. Phys. Chem. B* 109 (2005) 21900–21907.
- [65] X. Li, J.H. Ye, *J. Phys. Chem. C* 111 (2007) 13109–13116.
- [66] H. Park, W. Choi, *J. Phys. Chem. B* 109 (2005) 11667–11674.
- [67] J.C. Zhao, T.X. Wu, K.Q. Wu, K. Oikawa, H. Hidaka, N. Serpone, *Environ. Sci. Technol.* 32 (1998) 2394–2400.
- [68] T.X. Wu, G.M. Liu, J.C. Zhao, H. Hidaka, N. Serpone, *J. Phys. Chem. B* 102 (1998) 5845–5851.
- [69] T. Watanabe, T. Takizawa, K. Honda, *J. Phys. Chem.* 81 (1977) 1845–1851.
- [70] F. Chen, J.C. Zhao, H. Hidaka, *Int. J. Photoenergy* 5 (2003) 209–217.
- [71] S. Rehman, R. Ullah, A. Butt, N. Gohar, *J. Hazard. Mater.* 170 (2009) 560–569.
- [72] A.J. Nozik, *Ann. Rev. Phys. Chem.* 29 (1978) 189–222.
- [73] A. Mills, S. LeHunte, *J. Photochem. Photobiol. a-Chem.* 108 (1997) 1–35.
- [74] M. Gratzel, *Nature* 414 (2001) 338–344.
- [75] U.I. Gaya, A.H. Abdullah, *J. Photochem. Photobiol. C-Photochem. Rev.* 9 (2008) 1–12.
- [76] S. Sakthivel, H. Kisch, *Chemphyschem* 4 (2003) 487–490.
- [77] A.A. Tahir, K.G.U. Wijayantha, *J. Photochem. Photobiol. a-Chem.* 216 (2010) 119–125.
- [78] T. Tachikawa, M. Fujitsuka, T. Majima, *J. Phys. Chem. C* 111 (2007) 5259–5275.
- [79] H.J. Lv, L. Ma, P. Zeng, D.N. Ke, T.Y. Peng, *J. Mater. Chem.* 20 (2010) 3665–3672.
- [80] X.B. Chen, S.H. Shen, L.J. Guo, S.S. Mao, *Chem. Rev.* 110 (2010) 6503–6570.